

1    High-level cognition is supported by at least second order  
2    dynamic correlations in neural activity patterns

3    Lucy L. W. Owen<sup>1</sup>, Thomas H. Chang<sup>1,2</sup>, and Jeremy R. Manning<sup>1,†</sup>

<sup>1</sup>Department of Psychological and Brain Sciences,  
Dartmouth College, Hanover, NH

<sup>3</sup>Amazon.com, Seattle, WA

†Address correspondence to jeremy.r.manning@dartmouth.edu

4    August 29, 2019

5    **Abstract**

6    Our thoughts arise from coordinated patterns of interactions between brain structures that change  
7    with our ongoing experiences. High-order dynamic correlations in brain activity patterns reflect different  
8    subgraphs of the brain’s connectome that display homologous lower-level dynamic correlations. We tested  
9    the hypothesis that high-level cognition is supported by high-order dynamic correlations in brain activity  
10   patterns. We developed an approach to estimating high-order dynamic correlations in timeseries data,  
11   and we applied the approach to neuroimaging data collected as human participants either listened to a  
12   ten-minute story or a temporally scrambled version of the story, or underwent a resting state scan. We  
13   trained across-participants pattern classifiers to decode (in held-out data) when in the session each activity  
14   snapshot was collected. We found that classifiers trained to decode from high-order dynamic correlations  
15   yielded better performance on data collected as participants listened to the (unscrambled) story. By  
16   contrast, classifiers trained to decode data from scrambled versions of the story or during the resting  
17   state scan yielded the best performance when they were trained using first-order dynamic correlations  
18   or raw activity patterns. We suggest that as our thoughts become more complex, they are supported by  
19   higher-order patterns of dynamic network interactions throughout the brain.

20   **Introduction**

21   A central goal in cognitive neuroscience is to elucidate the *neural code*: the mapping between (a) mental  
22   states or cognitive representations and (b) neural activity patterns. One means of testing models of the  
23   neural code is to ask how accurately that model is able to “translate” neural activity patterns into known  
24   (or hypothesized) mental states or cognitive representations (e.g., Haxby et al., 2001; Huth et al., 2016, 2012;  
25   Kamitani & Tong, 2005; Mitchell et al., 2008; Nishimoto et al., 2011; Norman et al., 2006; Pereira et al., 2018;  
26   Tong & Pratte, 2012). Training decoding models on different types of neural features can also help to elucidate  
27   which specific aspects of neural activity patterns are informative about cognition– and, by extension, which  
28   types of neural activity patterns might comprise the neural code. For example, prior work has used region  
29   of interest analyses to estimate the anatomical locations of specific neural representations (e.g., Etzel et al.,  
30   2009), or to compare the relative contributions to the neural code of multivariate activity patterns versus

31 patterns of dynamic correlations between neural activity patterns (e.g., Fong et al., 2019; Manning et al.,  
32 2018). An emerging theme in this literature is that cognition is mediated by complex dynamic interactions  
33 between brain structures (Bassett et al., 2006; Demertzi et al., 2019; Sporns & Honey, 2006; Turk-Browne,  
34 2013).

35 Studies of the neural code to date have primarily focused on univariate or multivariate neural pat-  
36 terns (for review see , NormEtal06) or (more recently) on patterns of dynamic first-order correlations (i.e.,  
37 interactions between pairs of brain structures; Fong et al., 2019; Manning et al., 2018). We wondered what  
38 the future of this line of work might hold. For example, is the neural code mediated by higher-order  
39 interactions between brain structures? Second-order correlations reflect *homologous* patterns of correlation.  
40 In other words, if the changing patterns of correlations between two regions, *A* and *B*, are similar to those  
41 between two other regions, *C* and *D*, this would be reflected in the second-order correlations between (*A*–*B*)  
42 and (*C*–*D*). In this way, second-order correlations identify similarities and differences between subgraphs  
43 of the brain’s connectome. Analogously, third-order correlations reflect homologies between second-order  
44 correlations– i.e., homologous patterns of homologous interactions between brain regions. More generally,  
45 higher-order correlations reflect homologies between patterns of lower-order correlations. We can then ask:  
46 which “orders” of interaction are most reflective of high-level cognitive processes?

47 Another central question pertains to the extent to which the neural code is carried by activity patterns  
48 that directly reflect ongoing cognition (e.g., following Haxby et al., 2001; Norman et al., 2006), versus the  
49 dynamic properties of the network structure itself, independent of specific activity patterns in any given set  
50 of regions (e.g., following Bassett et al., 2006). For example, graph theoretic measures such as centrality and  
51 degree (Bullmore & Sporns, 2009) may be used to estimate how a given brain structure is “communicating”  
52 with other structures, independently of the specific neural representations carried by those structures. If  
53 one considers a brain region’s graph theoretic position in the network (e.g., its eigenvector centrality) as a  
54 dynamic property, one can compare how the positions of different regions are correlated, and/or how those  
55 patterns of correlations change over time. We can also compute higher-order patterns in these correlations  
56 to characterize homologous subgraphs in the connectome that display similar changes in their constituent  
57 brain structures’ interactions with the rest of the brain.

58 To gain insights into the above aspects of the neural code, we developed a computational framework  
59 for estimating dynamic high-order correlations in timeseries data. This framework provides an important  
60 advance, in that it enables us to examine patterns in higher-order correlations that are computationally  
61 intractable to estimate via conventional methods. Given a multivariate timeseries, our framework provides  
62 timepoint-by-timepoint estimates of the first-order correlations, second-order correlations, and so on (up to  
63 tenth-order correlations in this manuscript). Our approach combines a kernel-based method for computing

64 dynamic correlations in timeseries data with a dimensionality reduction step that projects the resulting dy-  
65 namic correlations into a low-dimensional space. We explored two dimensionality reduction approaches:  
66 principle components analysis (PCA; Pearson, 1901), which preserves an approximately invertable transfor-  
67 mation back to the original data; and a second non-invertible algorithm that explored patterns in eigenvector  
68 centrality (Landau, 1895). This latter approach characterizes correlations between each feature dimension's  
69 relative *position* in the network in favor of the specific activity histories of different features.

70 We validated our approach using synthetic data where the underlying correlations were known. We  
71 then applied our framework to a neuroimaging dataset collected as participants listened to either an audio  
72 recording of a ten-minute story or a temporally scrambled version of the story, or underwent a resting state  
73 scan (Simony et al., 2016). We used a subset of the data to train across-participant classifiers to decode  
74 listening times using a blend of neural features (comprising neural activity patterns, as well as different  
75 orders of correlations between those patterns that were inferred using our computational framework).  
76 We found that both the PCA-based and eigenvector centrality-based approaches yielded neural patterns  
77 that could be used to decode accurately. Both approaches also yielded the best decoding accuracy for  
78 data collected during (intact) story listening when high-order (PCA: second-order; eigenvector centrality:  
79 fourth-order) dynamic correlation patterns were included as features. When we trained classifiers on the  
80 scrambled stories or resting state data, only lower-order dynamic patterns were informative to the decoders.  
81 Taken together, our results indicate that high-level cognition is supported by high-order dynamic patterns  
82 of communication between brain structures.

## 83 Methods

84 Our general approach to comprises four general steps (Fig. 1). First, we derive a kernel-based approach  
85 to computing dynamic pairwise correlations in a  $T$  (timepoints) by  $K$  (features) multivariate timeseries,  
86  $\mathbf{X}_0$ . This yields a  $T$  by  $O(K^2)$  matrix of dynamic correlations,  $\mathbf{Y}_1$ , where each row comprises the upper  
87 triangle of the correlation matrix at a single timepoint, reshaped into a row vector (this reshaped vector is  
88  $(\frac{K^2-K}{2})$ -dimensional). Second, we apply a dimensionality reduction step to project the matrix of dynamic  
89 correlations back onto a  $K$ -dimensional space. This yields a  $T$  by  $K$  matrix,  $\mathbf{X}_1$ , that reflects an approximation  
90 of the dynamic correlations reflected in the original data. Third, we use repeated applications of the kernel-  
91 based dynamic correlation step to  $\mathbf{X}_n$  and the dimensionality reduction step to the resulting  $\mathbf{Y}_{n+1}$  to estimate  
92 high-order dynamnic correlations. Each application of these steps to a  $T$  by  $K$  time series  $\mathbf{X}_n$  yields a  $T$  by  $K$   
93 matrix,  $\mathbf{X}_{n+1}$ , that reflects the dynamic correlations between the columns of  $\mathbf{X}_n$ . In this way, we refer to  $n$  as  
94 the *order* of the timeseries, where  $\mathbf{X}_0$  (order 0) denotes the original data and  $\mathbf{X}_n$  denotes  $n^{\text{th}}$ -order dynamic

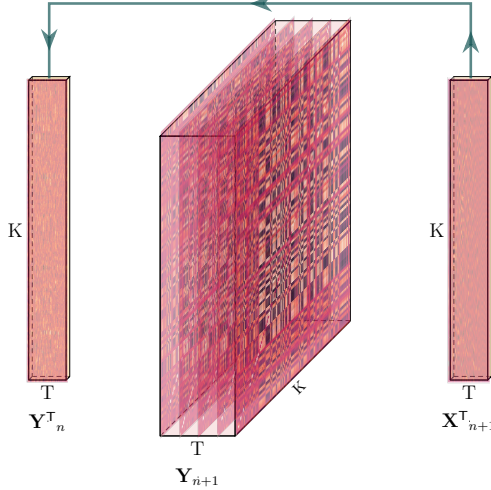


Figure 1: **Estimating dynamic high-order correlations.** Given a  $T$  by  $K$  matrix of multivariate timeseries data,  $\mathbf{Y}_n$  (where  $n \in \mathbb{N}, n \geq 0$ ), we use Equation 5 to compute a timeseries of  $K$  by  $K$  correlation matrices,  $\mathbf{Y}_{n+1}$ . We then approximate  $\mathbf{Y}_{n+1}$  with the  $T$  by  $K$  matrix  $\mathbf{X}_{n+1}$ . This process may be repeated to scalably estimate iteratively higher-order correlations in the data. Note that the transposes of  $\mathbf{Y}_n$  and  $\mathbf{X}_{n+1}$  are displayed in the figure for compactness.

95 correlations between the columns of  $\mathbf{X}_0$ . Finally, we use a cross-validation-based decoding approach to  
 96 evaluate how well information contained in a given order (or weighted mixture of orders) may be used  
 97 to decode relevant cognitive states. If including a given  $\mathbf{X}_n$  in the feature set yields higher classification  
 98 accuracy on held-out data, we interpret this as evidence that the given cognitive states are reflected in  
 99 patterns of  $n^{\text{th}}$ -order correlations.

## 100 Kernel-based approach for computing dynamic correlations

Given a matrix of observations, we can compute the (static) Pearson's correlation between any pair of columns,  $\mathbf{X}(\cdot, i)$  and  $\mathbf{X}(\cdot, j)$  using (Pearson, 1901):

$$\text{corr}(\mathbf{X}(\cdot, i), \mathbf{X}(\cdot, j)) = \frac{\sum_{t=1}^T (\mathbf{X}(t, i) - \bar{\mathbf{X}}(\cdot, i))(\mathbf{X}(t, j) - \bar{\mathbf{X}}(\cdot, j))}{\sqrt{\sum_{t=1}^T \sigma_{\mathbf{X}(\cdot, i)}^2 \sigma_{\mathbf{X}(\cdot, j)}^2}}, \text{ where} \quad (1)$$

$$\bar{\mathbf{X}}(\cdot, k) = \sum_{t=1}^T \mathbf{X}(t, k), \text{ and} \quad (2)$$

$$\sigma_{\mathbf{X}(\cdot, k)}^2 = \sum_{t=1}^T (\mathbf{X}(t, k) - \bar{\mathbf{X}}(\cdot, k))^2 \quad (3)$$

101 We can generalize this formula to compute time-varying correlations by incorporating a *kernel function* that  
 102 takes a time  $t$  as input, and returns how much the observed data at each timepoint  $\tau \in [-\infty, \infty]$  contributes

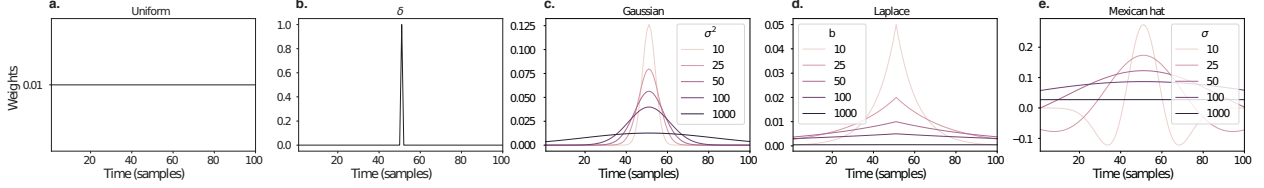


**Figure 2: Examples of kernel functions.** Each panel displays per-timepoint weights at  $t = 50$ , evaluated for 100 timepoints ( $\tau \in [1, \dots, 100]$ ). **a. Uniform kernel.** The weights are timepoint-invariant; observations at all timepoints are weighted equally, and do not change as a function of  $\tau$ . This is a special case of weight function that reduces dynamic correlations to static correlations. **b. Dirac  $\delta$  kernel.** Only the observation at timepoint  $t$  is given a non-zero weight (of 1). **c. Gaussian kernels.** Each kernel's weights fall off in time according to a Gaussian probability density function centered on time  $t$ . Weights derived using several different example variance parameters ( $\sigma^2$ ) are displayed. **d. Laplace kernels.** Each kernel's weights fall off in time according to a Laplace probability density function centered on time  $t$ . Weights derived using several different example scale parameters ( $b$ ) are displayed. **e. Mexican hat (Ricker wavelet) kernels.** Each kernel's weights fall off in time according to a Ricker wavelet centered on time  $t$ . This function highlights the *contrasts* between local versus surrounding activity patterns in estimating dynamic correlations. Weights derived using several different example width parameters ( $\sigma$ ) are displayed.

103 to the estimated instantaneous correlation at time  $t$  (Fig. 2).

Given a kernel function  $\kappa_t(\cdot)$  for timepoint  $t$ , evaluated at timepoints  $\tau \in [1, \dots, T]$ , we can update the static correlation formula in Equation 2 to estimate the *instantaneous correlation* at timepoint  $t$ :

$$\text{timecorr}_{\kappa_t}(\mathbf{X}(\cdot, i), \mathbf{X}(\cdot, j)) = \frac{\sum_{\tau=1}^T (\mathbf{X}(\tau, i) - \tilde{\mathbf{X}}_{\kappa_t}(i))(\mathbf{X}(\tau, j) - \tilde{\mathbf{X}}_{\kappa_t}(j))}{\sqrt{\sum_{\tau=1}^T \tilde{\sigma}_{\kappa_t}^2(\mathbf{X}(\tau, i)) \tilde{\sigma}_{\kappa_t}^2(\mathbf{X}(\tau, j))}}, \text{ where} \quad (4)$$

$$\tilde{\mathbf{X}}_{\kappa_t}(t, k) = \sum_{\tau=1}^T \kappa_t(\tau, k) \mathbf{X}(\tau, k), \quad (5)$$

$$\tilde{\sigma}_{\kappa_t}^2(\mathbf{X}(\cdot, k)) = \sum_{\tau=1}^T (\mathbf{X}(\tau, k) - \tilde{\mathbf{X}}_{\kappa_t}(t, k))^2. \quad (6)$$

104 Here  $\text{timecorr}(\mathbf{X}(\cdot, i), \mathbf{X}(\cdot, j), \kappa_t)$  reflects the correlation at time  $t$  between columns  $i$  and  $j$  of  $\mathbf{X}$ , estimated using  
105 the kernel  $\kappa_t$ .

#### 106 Dynamic inter-subject functional connectivity (DISFC)

Equation 5 provides a means of taking a single observation matrix,  $\mathbf{X}_n$  and estimating the dynamic correlations from moment to moment,  $\mathbf{Y}_{n+1}$ . Suppose that one has access to a set of multiple observation matrices that reflect the same phenomenon. For example, one might collect neuroimaging data from several experimental participants, as each participant performs the same task (or sequence of tasks). Let  $\mathbf{X}_n^1, \mathbf{X}_n^2, \dots, \mathbf{X}_n^P$  reflect the  $T$  by  $K$  observation matrices ( $n = 0$ ) or reduced correlation matrices ( $n > 0$ ) for each of  $P$  participants in an experiment. We can use *inter-subject functional connectivity* (ISFC; Simony et al., 2016)

to compute the degree of stimulus-driven correlations reflected in the multi-participant dataset at a given timepoint  $t$  using:

$$\bar{\mathbf{C}}(t) = M \left( R \left( \frac{1}{2P} \sum_{p=1}^P Z(Y_n^p(t))^T + Z(Y_n^p(t)) \right) \right), \quad (7)$$

where  $M$  extracts and vectorizes the diagonal and upper triangle of a symmetric matrix,  $Z$  is the Fisher  $z$ -transformation (Zar, 2010):

$$Z(r) = \frac{\log(1+r) - \log(1-r)}{2} \quad (8)$$

$R$  is the inverse of  $Z$ :

$$R(z) = \frac{\exp(2z-1)}{\exp(2z+1)}, \quad (9)$$

and  $\mathbf{Y}_n^p(t)$  denotes the correlation matrix (Eqn. 2) between each column of  $\mathbf{X}_n^p$  and each column of the average  $\mathbf{X}_n$  from all *other* participants,  $\bar{\mathbf{X}}_n^{\setminus p}$ :

$$\bar{\mathbf{X}}_n^{\setminus p} = R \left( \frac{1}{P-1} \sum_{q \in \setminus p} Z(\mathbf{X}_n^q) \right), \quad (10)$$

where  $\setminus p$  denotes the set of all participants other than participant  $p$ . In this way, the  $T$  by  $\frac{K^2-K}{2}$  DISFC matrix  $\bar{\mathbf{C}}$  provides a time-varying extension of the ISFC approach developed by Simony et al. (2016).

## Low-dimensional representations of dynamic correlations

Given a  $T$  by  $\frac{K^2-K}{2}$  matrix of dynamic correlations,  $\mathbf{Y}_n$ , we propose two general approaches to computing a  $T$  by  $K$  low-dimensional representation of these correlations,  $\mathbf{X}_n$ . The first approach uses dimensionality reduction algorithms to project  $\mathbf{Y}_n$  onto a  $K$ -dimensional space. The second approach uses graph-theoretic measures to characterize the relative positions of each feature ( $k \in [1, \dots, K]$ ) in the network defined by the correlation matrix at each timepoint.

### Dimensionality reduction-based approaches to computing $\mathbf{X}_n$

The modern library of dimensionality reduction algorithms include Principal Components Analysis (PCA; Pearson, 1901), Probabilistic PCA (PPCA; Tipping & Bishop, 1999), Exploratory Factor Analysis (EFA; Spearman, 1904), Independent Components Analysis (ICA; Comon et al., 1991; Jutten & Herault, 1991),

119  $t$ -Stochastic Neighbor Embedding ( $t$ -SNE; van der Maaten & Hinton, 2008), Uniform Manifold Approximation and Projection (UMAP; McInnes & Healy, 2018), non-negative matrix factorization (NMF; Lee & Seung, 1999), Topographic Factor Analysis (TFA) Manning et al. (2014), Hierarchical Topographic Factor analysis (HTFA) Manning et al. (2018), Topographic Latent Source Analysis (TLSA) Gershman et al. (2011), Dictionary learning (J. Mairal et al., 2009; J. B. Mairal et al., 2009), deep autoencoders (Hinton & Salakhutdinov, 2006), among others. While complete characterizations of each of these algorithms is beyond the scope of the present manuscript, the general intuition driving these approaches is to compute the  $T$  by  $I$  matrix,  $\mathbf{X}$ , that is closest to the original  $T$  by  $J$  matrix,  $\mathbf{Y}$ , where (typically)  $I \ll J$ . The different approaches place different constraints on what properties  $\mathbf{X}$  must satisfy and which aspects of the data are compared (and how) to characterize the match between  $\mathbf{X}$  and  $\mathbf{Y}$ .

129 Applying dimensionality reduction algorithms to  $\mathbf{Y}$  yields a  $\mathbf{X}$  whose columns reflect weighted combinations (or nonlinear transformations) of the original columns of  $\mathbf{Y}$ . This has two main consequences. First, 130 with each repeated dimensionality reduction, the resulting  $\mathbf{X}_n$  has lower and lower fidelity (with respect to 131 what the “true”  $\mathbf{Y}_n$  might have looked like without using dimensionality reduction to maintain scalability). 132 In other words, computing  $\mathbf{X}_n$  is a lossy operation. Second, whereas each columns of  $\mathbf{Y}_n$  may always be 133 mapped directly onto specific pairs of columns of  $\mathbf{Y}_{n-1}$ , the columns of  $\mathbf{X}_n$  reflect weighted combinations 134 and/or nonlinear transformations of the columns of  $\mathbf{Y}_n$ . Many dimensionality reduction algorithms are 135 invertable (or approximately invertable). However, attempting to map a given  $\mathbf{X}_n$  back onto the original 136 feature space of  $\mathbf{Y}_0$  will usually require  $O(TK^{2n})$  space and therefore quickly becomes intractable as  $n$  or  $K$  137 grow large.

### 139 **Graph theoretic approaches to computing $\mathbf{X}_n$**

140 The above dimensionality reduction approaches to approximating a given  $\mathbf{Y}_n$  with a lower-dimensional 141  $\mathbf{X}_n$  preserve a (potentially recombined and transformed) mapping back to the original data in  $\mathbf{Y}_0$ . We 142 also explore graph theoretic approaches that forgo a preserved mapping back to the original data in favor 143 of preserving each feature’s relative *position* in the broader network of interactions and connections. To 144 illustrate the distinction between the two general approaches we explore, suppose a network comprises 145 nodes  $A$ ,  $B$ , and  $C$ . If  $A$  and  $B$  exhibit uncorrelated activity patterns, the functional connection between 146 them will be (by definition) close to 0. However, if  $A$  and  $B$  each interact with  $C$  in similar ways, we might 147 attempt to capture those similarities using a measure that reflects the how  $A$  and  $B$  interact in the network.

148 In general, graph theoretic measures take as input a matrix of interactions (e.g., using the above notation, 149 an  $K$  by  $K$  correlation matrix or binarized correlation matrix reconstituted from a single timepoint’s row of

150  $\mathbf{Y}$ ) and return as output a set of  $K$  measures describing how each node (feature) sits within that correlation  
151 matrix with respect to the rest of the population. Widely used measures include betweenness centrality (the  
152 proportion of shortest paths between each pair of nodes in the population that involves the given node in  
153 question; e.g., Barthélémy, 2004; Freeman, 1977; Geisberger et al., 2008; Newman, 2005; Opsahl et al., 2010);  
154 diversity and dissimilarity (characterizations of how differently connected a given node is from others in  
155 the population; e.g., Lin, 2009; Rao, 1982; Ricotta & Szeidl, 2006); Eigenvector centrality and pagerank  
156 centrality (measures of how influential a given node is within the broader network; e.g., Bonacich, 2007;  
157 Halu et al., 2013; Lohmann et al., 2010; Newman, 2008); transfer entropy and flow coefficients (a measure  
158 of how much information is flowing from a given node to other nodes in the network; e.g., Honey et  
159 al., 2007; Schreiber, 2000);  $k$ -coreness centrality (a measure of the connectivity of a node within its local  
160 sub-graph; e.g., Alvarez-Hamelin et al., 2005; Christakis & Fowler, 2010); within-module degree (a measure  
161 of how many connections a node has to its close neighbors in the network; e.g., Rubinov & Sporns, 2010);  
162 participation coefficient (a measure of the diversity of a node's connections to different sub-graphs in the  
163 network; e.g., Rubinov & Sporns, 2010); and sub-graph centrality (a measure of a node's participation in  
164 all of the network's sub-graphs; e.g., Estrada & Rodríguez-Velázquez, 2005); among others.

165 For a given graph theoretic measure,  $\eta : \mathbb{R}^{K \times K} \rightarrow \mathbb{R}^K$ , we can use  $\eta$  to transform each row of  $\mathbf{Y}_n$  in a way  
166 that characterizes the corresponding graph-theoretic properties of each column. This results in a new  $T$  by  
167  $K$  matrix,  $\mathbf{X}_n$ , that reflects how the features reflected in the columns of  $\mathbf{Y}_n$  participate in the network during  
168 each timepoint (row).

## 169 Higher-order correlations

170 Because  $\mathbf{X}_n$  has the same shape as the original data  $\mathbf{X}_0$ , approximating  $\mathbf{Y}_n$  with a lower-dimensional  $\mathbf{X}_n$   
171 enables us to estimate high-order dynamic correlations in a scalable way. Given a  $T$  by  $K$  input matrix, the  
172 output of Equation 5 requires  $O(TK^2)$  space to store. Repeated applications of Equation 5 (i.e., computing  
173 dynamic correlations between the columns of the outputted dynamic correlation matrix) each require  
174 exponentially more space; in general the  $n^{\text{th}}$ -order dynamic correlations of a  $T$  by  $K$  timeseries occupies  
175  $O(TK^{2n})$  space. However, when we approximate or summarize the output of Equation 5 with a  $T$  by  $K$  matrix  
176 (as described above), it becomes feasible to compute even very high-order correlations in high-dimensional  
177 data. Specifically, approximating the  $n^{\text{th}}$ -order dynamic correlations of a  $T$  by  $K$  timeseries requires only  
178  $O(TK^2)$  additional space— the same as would be required to compute first-order dynamic correlations. In  
179 other words, the space required to store  $n + 1$  multivariate timeseries reflecting up to  $n^{\text{th}}$  order correlations  
180 in the original data scales linearly with  $n$  using our approach (Fig. 1).

181 **Data**

182 We examined two types of data: synthetic data and human functional neuroimaging data. We constructed  
183 and leveraged the synthetic data to evaluate our general approach. Specifically, we tested how well  
184 Equation 5 could be used to recover known dynamic correlations using different choices of kernel ( $\kappa$ ; Fig. 2),  
185 for each of several synthetic datasets that exhibited different temporal properties. We applied our approach  
186 to a functional neuroimaging dataset to test the hypothesis that ongoing cognitive processing is reflected  
187 in high-order dynamic correlations. We used an across-participant classification test to estimate whether  
188 dynamic correlations of different orders contain information about which timepoint in a story participants  
189 were listening to.

190 **Synthetic data**

191 We constructed a total of 40 multivariate timeseries, collectively reflecting a total of 4 different patterns of  
192 dynamic correlations (i.e., 10 datasets reflecting each type of dynamic pattern). Each timeseries comprised  
193 50 features (dimensions) that varied over 300 timepoints. The observations at each timepoint were drawn  
194 from a zero-mean multivariate Gaussian distribution with a covariance matrix defined for each timepoint  
195 as described below. We drew the observations at each timepoint independently from the draws at all other  
196 timepoints; in other words, for each observation  $s_t \sim \mathcal{N}(\mathbf{0}, \Sigma_t)$  at timepoint  $t$ ,  $p(s_t) = p(s_t|p_{\setminus t})$ .

**Constant.** We generated data with stable underlying correlations to evaluate how Equation 5 characterized correlation “dynamics” when the ground truth correlations were static. We constructed 10 multivariate timeseries, whose observations were each drawn from a single (stable) Gaussian distribution. For each dataset, we constructed a random covariance matrix,  $\Sigma_m$ :

$$\mathbf{C}(i, j) \sim \mathcal{N}(0, 1) \quad (11)$$

$$\Sigma_m = \mathbf{C}\mathbf{C}^\top, \text{ where} \quad (12)$$

197  $i, j \in [1, 2, \dots, 50]$ . In other words, all of the observations (for each of the 300 timepoints) within each dataset  
198 were drawn from a multivariate Gaussian distribution with the same covariance matrix, and the 10 datasets  
199 each used a different covariance matrix.

200 **Random.** We generated a second set of 10 synthetic datasets whose observations at each timepoint were  
201 drawn from a Gaussian distribution with a new randomly constructed (using Eqn. 12) covariance matrix.  
202 Because each timepoint’s covariance matrix was drawn independently of the covariance matrices for all

203 other timepoints, these datasets provided a test of reconstruction accuracy in the absence of any meaningful  
204 underlying temporal structure in the dynamic correlations underlying the data.

**Ramping.** We generated a third set of 10 synthetic datasets whose underlying correlations changed gradually over time. For each dataset, we constructed two *anchor* correlation matrices using Equation 12,  $\Sigma_{\text{start}}$  and  $\Sigma_{\text{end}}$ . For each of the 300 timepoints in each dataset, we drew the observations from a multivariate Gaussian distribution whose covariance matrix at each timepoint  $t \in [0, \dots, 299]$  was given by

$$\Sigma_t = \left(1 - \frac{1-t}{299}\right) \Sigma_{\text{start}} + \frac{t}{299} \Sigma_{\text{end}}. \quad (13)$$

205 The gradually changing correlations underlying these datasets allow us to evaluate the recovery of dynamic  
206 correlations when each timepoint's correlation matrix is unique (as in the random datasets), but where the  
207 correlation dynamics are structured.

208 **Event.** We generated a fourth set of 10 synthetic datasets whose underlying correlation matrices exhibited  
209 prolonged intervals of stability, interspersed with abrupt changes. For each dataset, we used Equation ??  
210 to generate 5 random covariance matrices. We constructed a timeseries where each set of 60 consecutive  
211 samples was drawn from a Gaussian with the same covariance matrix. These datasets were intended to  
212 simulate a system that undergoes occasional abrupt state changes.

213 **JRM STOPPED HERE**

214 **Functional neuroimaging data collected during story listening**

215 **Estimating high-order correlations in neuroimaging data**

216 **Temporal decoding**

217 **Forward inference, cross validation, and feature selection**

218 **Identifying robust decoding results**

219 **Reverse inference**

220 **JRM OUTLINE STOPPED HERE**

221 **Evaluation metrics**

222 We evaluate our approach to extracting dynamic correlations and higher-order correlations using several  
223 metrics detailed next. First, we generated synthetic data using known time-varying correlations, and then  
224 we evaluated the fidelity with which Equation 5 could recover those correlations (for synthetic datasets  
225 with different properties, and using different kernels to define the weights; Fig. 2). We then turned to a  
226 series of analyses on a (real) neuroimaging dataset where the ground truth correlations were *not* known.  
227 We evaluated whether the recovered correlations could be used to accurately label held-out neuroimaging  
228 data with the time at which it was collected. We used this latter evaluations (using timewindow decoding)  
229 as a proxy for gauging how much explanatory power the recovered correlations held with respect to the  
230 observed data.

231 **Generating synthetic data**

232 To explore recovery of a constant covariance (Fig. 3, a.), we generated synthetic data sampled from a constant  
233 covariance matrix. To do this, we created one random covariance matrix,  $K$ , with 50 features, and for each  
234 of the 300 timepoints we sampled from a Gaussian distribution centered on  $K$ . Similarly, we generated  
235 synthetic data sampled from a random covariance matrix (Fig. 3, b.) by creating a new random covariance  
236 matrix  $K(t)$ , for each of the 300 timepoints and sampled from a Gaussian distribution centered on  $K(t)$ .

To generate synthetic data from a dynamically changing covariance matrix (Fig. 3, c.), we generated two  
random covariance matrices,  $K_1$  and  $K_2$ . We then computed a weighted average covariance matrix for each  
of the 300 timepoint,  $K(t)$ , by taking the linearly spaced weights ( $w$ ) of the two random matrices,

$$K(t) = w(t) * K_1 + (1 - w(t)) * K_2, \quad (14)$$

$$(15)$$

237 and for each of the 300 timepoints sampled from a Gaussian distribution centered on  $K(t)$ .

238 Lastly, for the synthetic data containing block structure (Fig. 3, d.), we followed the same process of  
239 creating synthetic data sampled from a constant covariance matrix (see above) but sampled from a new  
240 random covariance matrix after 60 consecutive timepoints. We then pieced the blocks together to create a  
241 synthetic dataset with 300 total timepoints but drawn from 5 separate covariance matrices.

242 **Recovery of ground truth parameters from synthetic data**

243 We applied timecorr, using delta and gaussian (width = 10) kernels Fig. 2) to each of these synthetic datasets,  
244 then correlated each recovered correlation matrix with the ground truth. We repeated this process 10 times  
245 and explored how recovery varies with the kernel and the specific structure of the data. For the ramping  
246 synthetic dataset (Fig. 3, c.) and for the block synthetic dataset (Fig. 3, d.) we made further comparisons  
247 of the timecorr recovered correlation matrices. We compared the ramping recovered correlation matrices to  
248 only the first random covariance matrix  $K_1$  (First, Fig. 3, c.) and to only the last random covariance matrix  
249  $K_2$  (Last, Fig. 3, c.) from Equation 15. We also compared the block recovered correlation matrices in to the  
250 block specific covariance matrix (Block 1-5, Fig. 3, d.).

251 **Timepoint decoding**

252 To explore how higher-order structure varies with stimulus structure and complexity, we used a previous  
253 neuroimaging dataset Simony et al. (2016) in which participants listened to an audio recording of a story;  
254 36 participants listen to an intact version of the story, 17 participants listen to time-scrambled recordings of  
255 the same story where paragraphs were scrambled, 36 participants listen to word-scrambled version and 36  
256 participants lay in rest condition.

257 Prior work has shown participants share similar neural responses to richly structured stimuli when  
258 compared to stimuli with less structure. To assess whether the moment-by-moment higher order correlations  
259 were reliably preserved across participants, we used inter-subject functional connectivity (ISFC) to isolate  
260 the time-varying correlational structure (functional connectivity patterns that were specifically driven by  
261 the story participants listened to. Following the analyses conducted by (HTFA) Manning et al. (2018), we  
262 first applied *hierarchical topographic factor analysis* (HTFA) to the fMRI datasets to obtain a time series of  
263 700 node activities for every participant. We then computed the dynamic weighted ISFC using a range of  
264 kernels and widths. Specifically, we used Gaussian, Laplace, and mexican hat kernels, as well as widths of  
265 5, 10, 20, and 50. We then approximated these dynamic correlation using two reduction measures, PCA and  
266 eigenvector centrality, and computed the dynamic weighted ISFC on the approximations. We repeated this  
267 process up to 10th order approximated correlations.

268 To assess decoding accuracy, we randomly divided participants for each stimulus into training and  
269 testing groups. For the zeroth order, we computed the mean factor activity for each group. For all subsequent  
270 orders up to the tenth order, we computed the mean approximated dynamic ISFC of factor activity for each  
271 group. To assess how additional higher-order correlations contribute to decoding accuracy, for each order  
272 we included a weighted-mixutre (described below) of the activity patterns of all previous orders. For each

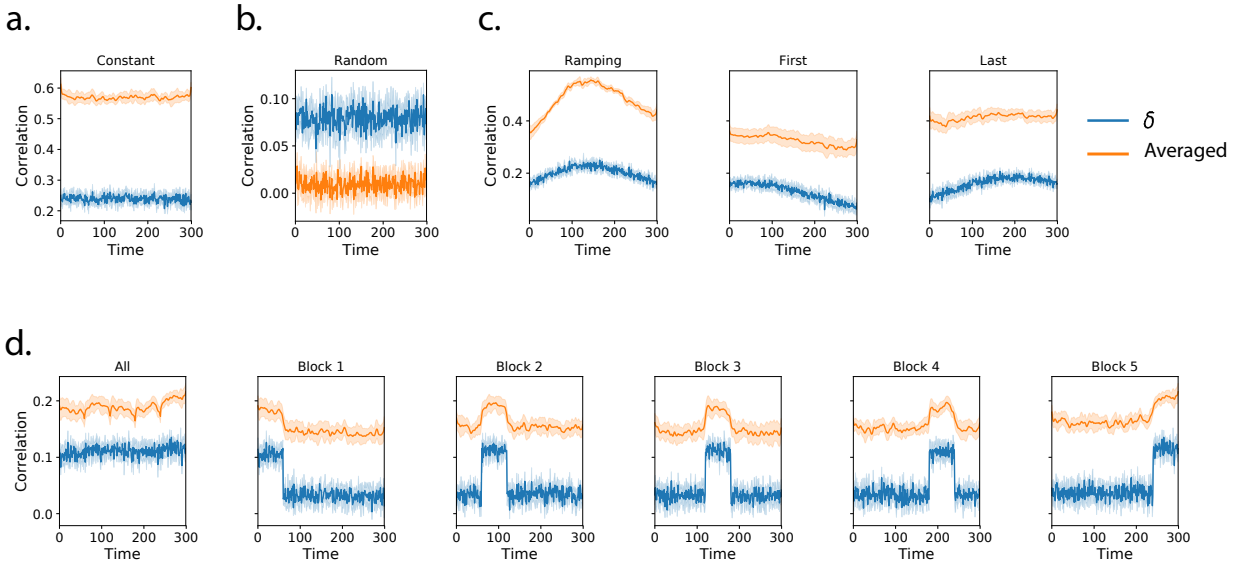


**Figure 3: Dynamic correlation recovery with synthetic data.** Using synthetic data containing different underlying correlational structure, we test how well we can recover dynamic correlation matrices using different kernels when compared to ground truth. We compare the results using a delta kernel with averaged results from several kernels (Gaussian, Laplace, and mexican hat) and several widths (5, 10, 20, and 50). We plot recovery using of datasets containing the following underlying structure: **a. Constant.** **b. Random.** **c. Ramping.** **d. Block.**

273 group of participants in turn, we compared these activity patterns (using Pearson correlations) to estimate  
 274 the story times each pattern corresponded to. Specifically, we asked, for each timepoint: what are the  
 275 correlations between the first group's and second group's activity patterns at each order. We note that the  
 276 decoding test we used is a conservative in which we count a timepoint label as incorrect if it is not an exact  
 277 match.

278 For each order we obtained the weighted-mixture of the correlation matrices for the current order and  
 279 all previous orders using mixing parameter,  $\phi$ , where  $0 < \phi < 1$  reflects a weighted mixture of order based  
 280 decoding Fig. 4 Panel c.). We calculated  $\phi$ , by subdividing the training group and using the quasi-Newton  
 281 method of Broyden, Fletcher, Goldfarb, and Shanno (BFGS (Nocedal & Wright, 2006)) for optimization. We  
 282 repeated this cross-validation process 10 times for each parameter set.

## 283 Results

### 284 Synthetic data

285 To assess the performance of dynamic correlation recovery using timecorr, we varied width the kernel and  
 286 the specific structure of the data. We applied timecorr, using delta and gaussian kernels Fig. 2) to each of

287 the following synthetic datasets: constant, random, ramping, and block. We then correlated each recovered  
288 correlation matrix with the ground truth.

289 For the constant synthetic dataset, a gaussian kernel (width=10) outperformed the delta kernel (Fig. 3,  
290 a.). This is in contrast with the random synthetic dataset, for which the delta kernel best captures the rapidly  
291 changing structure (Fig. 3, b.). For the ramping synthetic dataset, the slow changing strucutre within the  
292 data is best captured by the gaussian kernel and the best recovery occurs in the middle (Ramping, Fig. 3,  
293 c.). In addition to comparing the timecorr recovered correlation matrices to the ground truth, we further  
294 compared the ramping recovered correlation matrices to only the first random covariance matrix  $K_1$  (First,  
295 Fig. 3, c.) and to only the last random covariance matrix  $K_2$  (Last, Fig. 3, c.), both of which perform best at  
296 the beginning and end respectively.

297 Similary for the block sythetic dataset, we compared the timecorr recovered correlation matrices to  
298 the ground truth as well as to each block-specific covariance matrix (Block 1-5, Fig. 3, d.). Although the  
299 structure is changing by block, the gaussian kernel once again outperforms the delta kernel. Performance  
300 does however drop near even boundaries for when using the gaussian kernel.

301 **Neuroimaging dataset (Simony et al., 2016)**

302 For our decoding analysis, we used HTFA-derived node activities Manning et al. (2018) from fMRI data  
303 collected as participants listened to an audio recording of a story (intact condition; 36 participants), lis-  
304 tened to time scrambled recordings of the same story (17 participants in the paragraph-scrambled condition  
305 listened to the paragraphs in a randomized order and 36 in the word-scrambled condition listened to  
306 the words in a randomized order), or lay resting with their eyes open in the scanner (rest condition; 36  
307 participants). We sought to demonstrate how higher-order correlations may be used to examine dynamic  
308 interactions of brain patterns in (real) multi-subject fMRI datasets. This story listening dataset was col-  
309 lected as part of a separate study, where the full imaging parameters, image preprocessing methods, and  
310 experimental details may be found (Simony et al., 2016). The dataset is available at <http://arks.princeton.edu/ark:/88435/dsp015d86p269k>.

312 We next evaluated if our model of high-order correlations in brain activity can capture cognitively  
313 relevant brain patterns. We performed a decoding analysis, using cross validation to estimate (using other  
314 participants' data) which parts of the story each weighted-mixture of higher-order brain activity pattern  
315 corresponded to (see *Materials and methods*). We note that our primary goal was not to achieve perfect  
316 decoding accuracy, but rather to use decoding accuracy as a benchmark for assessing whether different  
317 neural features specifically capture cognitively relevant brain patterns.

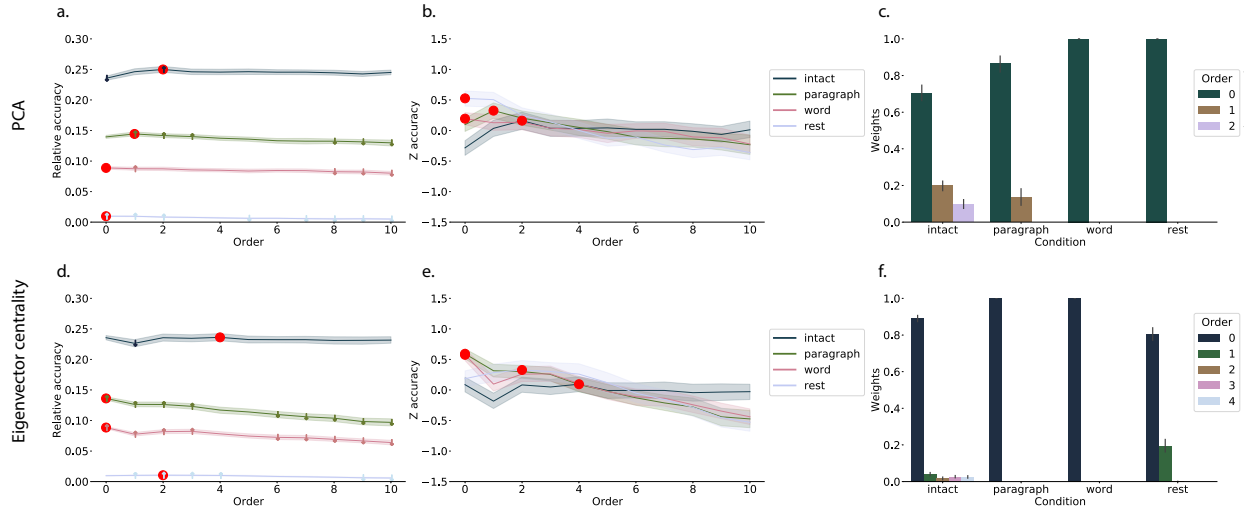


Figure 4: **Decoding by order.** **a.&d. Relative decoding accuracy by order.** Ribbons of each color display cross-validated decoding performance averaged over all parameters for each condition (intact, paragraph, word, and rest) using PCA (a.) or eigenvector centrality (d.) to approximate correlations. Decoders were trained using increasingly more higher-order information and this ribbons are displayed relative to chance at 0. The red dots indicates maximum decoding accuracy for each condition. **b.&e. Z-transformed decoding accuracy by order.** We Z-transformed the decoding accuracy by order to better visualize the order with the maximum decoding accuracy for each condition using PCA (b.) or eigenvector centrality (e.) to approximate correlations. **c.&f. Optimized weights.** Bar heights indicate the optimized mixing parameter  $\phi$  of each contributing order up to and including the order with the maximum decoding accuracy for each contributing order using PCA (c.) or eigenvector centrality (f.) to approximate correlations. For the order with maximum decoding accuracy by condition, we show barplots of the optimized weights  $\phi$  for each contributing order.

318 Separately for each experimental condition, we divided participants into two groups. For the zeroth  
319 order, we computed the mean factor activity for each group. For all subsequent orders up to the tenth  
320 order, we computed the mean approximated dynamic ISFC of factor activity for each group (see *Materials*  
321 and *methods*), and combined in a weighted mixutre with all previous orders (i.e. cross-validation for the  
322 second order contained a weighted-mixture of zeroth, first, and second order (Fig. 4, c.&f.). For each  
323 order, we correlated the group 1 activity patterns with group 2 activity patterns. We then subdivided  
324 the group 1 to obtain an optimal weighting parameter for each order's correlation matrix using the same  
325 cross validation method. We used the optimal weighting parameters to obtain a weighted-mixture (see  
326 *Materials and methods*) of each order's correlation matrix. Using these correlations, we labeled the group 1  
327 timepoints using the group 2 timepoints with which they were most highly correlated; we then computed  
328 the proportion of correctly labeled group 1 timepoints. (We also performed the symmetric analysis whereby  
329 we labeled the group 2 timepoints using the group 1 timepoints as a template.) We repeated this procedure  
330 100 times (randomly re-assigning participants to the two groups each time) to obtain a distribution of  
331 decoding accuracies for each experimental condition. There were 272 timepoints for paragraph condition,  
332 300 timepoints for intact and word conditions, and 400 timepoints for rest condition, so chance performance  
333 on this decoding test is was  $\frac{1}{272}$ ,  $\frac{1}{300}$ , and  $\frac{1}{400}$  respectively.

334 We repeated this process for each set of parameters, varying kernel type and width, and averaged over the  
335 reduction technique used to approximate the higher-order correlations (PCA Fig. 4, a.-c. and eigenvector  
336 centrality Fig. 4, d.-f.). Since there is no ground truth in these analyses, and we did not know which  
337 parameters best capture the data, we instead report a robustness search by averaging over the parameters  
338 and reporting which results consistently showed up across all parameters.

339 The two methods used to approximate the higher-order correlations (PCA Fig. 4, a.-c. and eigenvector  
340 centrality Fig. 4, d.-f.) capture different facets of the activity patterns. Using PCA, the higher-order  
341 correlations are all linked to the original activity patterns, whereas eigenvectory centrality breaks the  
342 immediate link with specific brain areas and instead characterizes the position of the nodes in the network  
343 that are similar over time.

344 We found for both PCA and eigenvector centrality, during the intact condition in the experiment,  
345 classifiers that incorporated higher-order correlations yielded consistently higher accuracy than classifiers  
346 trained only on lower-order patterns (Fig. 4, a.&d.). We plot the average correlations for up to the fourth  
347 order for the intact condition (Fig. 5) representing the degree of agreement by location pair over time. By  
348 contrast, we found that incorporating higher-order (greater than first order) correlations did not further  
349 improve decoding accuracy for the other listening conditions or rest condition. This suggests that the  
350 cognitive processing that supported the most cognitively rich condition involved higher-order network

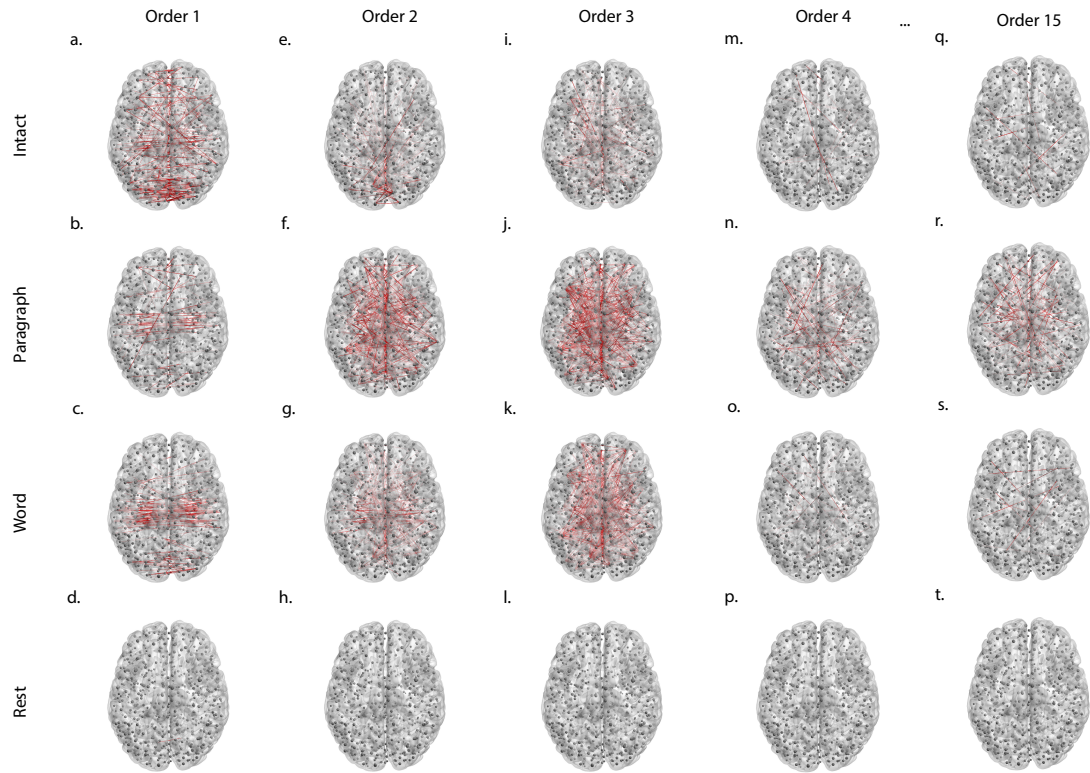


**Figure 5: Average correlations by order for the intact listening condition.** Using eigenvector centrality to approximate higher-order correlations for the intact, paragraph scrambled, word scrambled, and rest condition. We plot the strongest 50% absolute value mean correlation for **a.-d. first order, e.-h. second order, i.-l. third order, and m.-p. fourth order**, representing the degree of agreement by location pair over time. To demonstrate how this method is computationally scalable, we also approximated **a.-d. fifteenth order** dynamic correlation, which would be possible to compute using conventional methods since it would require more bits to represent the solution than there are molecules in the universe.

351 dynamics.

## 352 Discussion

353 • Methods advances: kernel-based dynamic correlations, extension to dynamic ISFC, efficient method  
354 for estimating high-order dynamic correlations, identifying robust results by averaging

355 • Discoveries:

- 356 – Dimensionality reduction and graph theoretic approaches give different insights into the data  
357 and identify different patterns as being relevant to cognition (different peak orders).
- 358 – An insight common to both approaches is that high-order (greater than first order) dynamic  
359 correlations are informative about ongoing high-level cognitive processing. As the level of  
360 cognitive processing decreases, cognition is reflected by lower-order correlations.
- 361 – Correlations at different orders are also associated with different networks of brain regions. How-  
362 ever, which networks reflect which types of interactions depends on the current task. In general,  
363 lower order correlations during auditory listening reflect processing of low-level (auditory) fea-  
364 tures; mid-order correlations reflect speech and linguistic processing; higher-order correlations  
365 reflect across-sensory integration (e.g. ties to visual areas) and cognitive control areas. This  
366 hierarchy dissolves during lower-order cognitive processing.

367 Based on prior work (Demertzis et al., 2019) and following the direction of the field (Turk-Browne, 2013)  
368 we think our thoughts might be encoded in dynamic network patterns, and possibly higher order network  
369 patterns (Fig. 6). We sought to test this hypothesis by developing an approach to inferring high-order  
370 network dynamics from timeseries data.

371 One challenge in studying dynamic interactions is the computational resources required to calculate  
372 higher-order correlations. We developed a computationally tractable model of network dynamics (Fig. 1)  
373 that takes in a feature timeseries and outputs approximated first-order dynamics (i.e., dynamic functional  
374 correlations), second-order dynamics (reflecting homologous networks that dynamically form and disperse),  
375 and higher-order network dynamics (up to tenth-order dynamic correlations).

376 We first validated our model using synthetic data, and explored how recovery varied with different  
377 underlying data structures and kernels. We then applied the approach to an fMRI dataset (Simony et al.,  
378 2016) in which participants listened to an audio recording of a story, as well as scrambled versions of the  
379 same story (where the scrambling was applied at different temporal scales). We trained classifiers to take

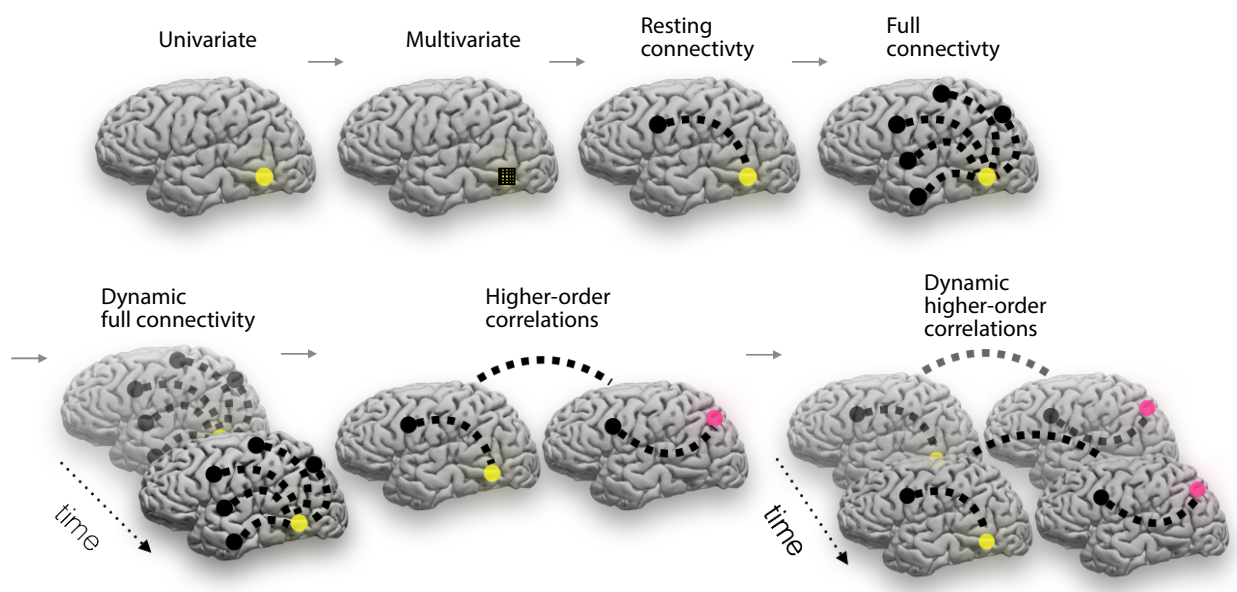


**Figure 6: Direction of the field (adapted from (Turk-Browne, 2013)).** The evolution of fMRI analyses started with univariate activation, which refers to the average amplitude of BOLD activity evoked by events of an experimental condition. Next, multivariate classifiers are trained on patterns of activation across voxels to decode distributed representations for specific events. The next, resting connectivity, is the temporal correlation of one or more seed regions with the remainder of the brain during rest. Additionally, task-based connectivity examines how these correlations differ by cognitive state. Following this increasing trajectory of increasing complexity, full connectivity considers all pairwise correlations in the brain, most commonly at rest. Next, dynamic full connectivity considers how full connectivity changes over time. Continuing this line of reasoning, we expect higher-order network dynamics might provide even richer insights into the neural basis of cognition.

380 the output of the model and decode the timepoint in the story (or scrambled story) that the participants  
381 were listening to. We found that, during the intact listening condition in the experiment, classifiers that  
382 incorporated higher-order correlations yielded consistently higher accuracy than classifiers trained only  
383 on lower-order patterns (Fig. 4, a.&d.). By contrast, these higher-order correlations were not necessary  
384 to support decoding the other listening conditions and (minimally above chance) during a control rest  
385 condition. This suggests that the cognitive processing that supported the most cognitively rich listening  
386 conditions involved second-order (or higher) network dynamics.

387 Although we found decoding accuracy was best when incorporating higher-order network dynamics  
388 for all but rest condition, it is unclear if this is a product of the brain or the data collection technique. It could  
389 be that the brain is second-order or it could be that fMRI can only reliably give second-order interactions.  
390 Exploring this method with other data collection technique will be important to disentangle this question.

## 391 **Concluding remarks**

392 How can we better understand how brain patterns change over time? How can we quantify the potential  
393 network dynamics that might be driving these changes? One way to judge the techniques of the future is  
394 to look at the trajectory of the fMRI field so far has taken so far (Fig. 1). The field started with univariate  
395 activation, measuring the average activity for each voxel. Analyses of multivariate activation followed,  
396 looking at spatial patterns of activity over voxels. Next, correlations of activity were explored, first with  
397 measures like resting connectivity that take temporal correlation between a seed voxel and all other voxels  
398 then with full connectivity that measure all pairwise correlations. Additionally, this path of increasing  
399 complexity also moved from static to dynamic measurements. One logical next step in this trajectory would  
400 be dynamic higher-order correlations. We have created a method to support these calculations by scalably  
401 approximating dynamic higher-order correlations.

## 402 **Acknowledgements**

403 We acknowledge discussions with Luke Chang, Hany Farid, Paxton Fitzpatrick, Andrew Heusser, Eshin  
404 Jolly, Qiang Liu, Matthijs van der Meer, Judith Mildner, Gina Notaro, Stephen Satterthwaite, Emily Whitaker,  
405 Weizhen Xie, and Kirsten Ziman. Our work was supported in part by NSF EPSCoR Award Number 1632738  
406 to J.R.M. and by a sub-award of DARPA RAM Cooperative Agreement N66001-14-2-4-032 to J.R.M. The  
407 content is solely the responsibility of the authors and does not necessarily represent the official views of our  
408 supporting organizations.

409 **Author contributions**

410 Concept: J.R.M. Implementation: T.H.C., L.L.W.O., and J.R.M. Analyses: L.L.W.O and J.R.M.

411 **References**

- 412 Alvarez-Hamelin, I., Dall'Asta, L., Barrat, A., & Vespignani, A. (2005). *k*-corr decomposition: a tool for the  
413 visualiztion of large scale networks. *arXiv*, cs/0504107v2.
- 414 Barthélemy, M. (2004). Betweenness centrality in large complex networks. *European Physical Journal B*, 38,  
415 163–168.
- 416 Bassett, D., Meyer-Lindenberg, A., Achard, S., Duke, T., & Bullmore, E. (2006, December). Adaptive  
417 reconfiguration of fractal small-world human brain functional networks. *Proceedings of the National  
418 Academy of Sciences, USA*, 103(51), 19518–23.
- 419 Bonacich, P. (2007). Some unique properties of eigenvector centrality. *Social Networks*, 29(4), 555–564.
- 420 Bullmore, E., & Sporns, O. (2009). Complex brain networks: graph theoretical analysis of structural and  
421 functional systems. *Nature Reviews Neuroscience*, 10(3), 186–198.
- 422 Christakis, N. A., & Fowler, J. H. (2010). Social network sensors for early detection of contagious outbreaks.  
423 *PLoS One*, 5(9), e12948.
- 424 Comon, P., Jutten, C., & Herault, J. (1991). Blind separation of sources, part II: Problems statement. *Signal  
425 Processing*, 24(1), 11 - 20.
- 426 Demertzi, A., Tagliazucchi, E., Dehaene, S., Deco, G., Barttfeld, P., Raimondo, F., ... Sitt, J. D. (2019). Human  
427 consciousness is supported by dynamic complex patterns of brain signal coordination. *Science Advances*,  
428 5(2), eaat7603.
- 429 Estrada, E., & Rodríguez-Velázquez, J. A. (2005). Subgraph centrality in complex networks. *Physical Review  
430 E*, 71(5), 056103.
- 431 Etzel, J. A., Gazzola, V., & Keysers, C. (2009). An introduction to anatomical ROI-based fMRI classification.  
432 *Brain Research*, 1282, 114–125.
- 433 Fong, A. H. C., Yoo, K., Rosenberg, M. D., Zhang, S., Li, C.-S. R., Scheinost, D., ... Chun, M. M. (2019).  
434 Dynamic functional connectivity during task performance and rest predictsindividual differences in  
435 attention across studies. *NeuroImage*, 188, 14–25.

- 436 Freeman, L. C. (1977). A set of measures of centrality based on betweenness. *Sociometry*, 40(1), 35–41.
- 437 Geisberger, R., Sanders, P., & Schultes, D. (2008). Better approximation of betweenness centrality. *Proceedings*  
438 *of the meeting on Algorithm Engineering and Experiments*, 90–100.
- 439 Gershman, S., Blei, D., Pereira, F., & Norman, K. (2011). A topographic latent source model for fMRI data.  
440 *NeuroImage*, 57, 89–100.
- 441 Halu, A., Mondragón, R. J., Panzarasa, P., & Bianconi, G. (2013). Multiplex PageRank. *PLoS One*, 8(10),  
442 e78293.
- 443 Haxby, J. V., Gobbini, M. I., Furey, M. L., Ishai, A., Schouten, J. L., & Pietrini, P. (2001). Distributed and  
444 overlapping representations of faces and objects in ventral temporal cortex. *Science*, 293, 2425–2430.
- 445 Hinton, G. E., & Salakhutdinov, R. R. (2006). Reducing the dimensionality of data with neural networks.  
446 *Science*, 313(5786), 504–507.
- 447 Honey, C. J., Kötter, R., Breakspear, M., & Sporns, O. (2007). Network structure of cerebral cortex shapes  
448 functional connectivity on multiple time scales. *Proceedings of the National Academy of Science USA*, 104(24),  
449 10240–10245.
- 450 Huth, A. G., de Heer, W. A., Griffiths, T. L., Theunissen, F. E., & Gallant, J. L. (2016). Natural speech reveals  
451 the semantic maps that tile human cerebral cortex. *Nature*, 532, 453–458.
- 452 Huth, A. G., Nisimoto, S., Vu, A. T., & Gallant, J. L. (2012). A continuous semantic space describes  
453 the representation of thousands of object and action categories across the human brain. *Neuron*, 76(6),  
454 1210–1224.
- 455 Jutten, C., & Herault, J. (1991). Blind separation of sources, part I: An adaptive algorithm based on  
456 neuromimetic architecture. *Signal Processing*, 24(1), 1–10.
- 457 Kamitani, Y., & Tong, F. (2005). Decoding the visual and subjective contents of the human brain. *Nature*  
458 *Neuroscience*, 8, 679–685.
- 459 Landau, E. (1895). Zur relativen Wertbemessung der Turnierresultate. *Deutsches Wochenschach*, 11, 366–369.
- 460 Lee, D. D., & Seung, H. S. (1999). Learning the parts of objects by non-negative matrix factorization. *Nature*,  
461 401, 788–791.
- 462 Lin, J. (2009). Divergence measures based on the Shannon entropy. *IEEE Transactions on Information Theory*,  
463 37(1), 145–151.

- 464 Lohmann, G., Margulies, D. S., Horstmann, A., Pleger, B., Lepsius, J., Goldhahn, D., ... Turner, R. (2010).  
465 Eigenvector centrality mapping for analyzing connectivity patterns in fMRI data of the human brain.  
466 *PLoS One*, 5(4), e10232.
- 467 Mairal, J., Ponce, J., Sapiro, G., Zisserman, A., & Bach, F. R. (2009). Supervised dictionary learning. *Advances  
468 in Neural Information Processing Systems*, 1033–1040.
- 469 Mairal, J. B., Bach, F., Ponce, J., & Sapiro, G. (2009). Online dictionary learning for sparse coding. *Proceedings  
470 of the 26th annual international conference on machine learning*, 689–696.
- 471 Manning, J. R., Ranganath, R., Norman, K. A., & Blei, D. M. (2014). Topographic factor analysis: a Bayesian  
472 model for inferring brain networks from neural data. *PLoS One*, 9(5), e94914.
- 473 Manning, J. R., Zhu, X., Willke, T. L., Ranganath, R., Stachenfeld, K., Hasson, U., ... Norman, K. A. (2018).  
474 A probabilistic approach to discovering dynamic full-brain functional connectivity patterns. *NeuroImage*,  
475 180, 243–252.
- 476 McInnes, L., & Healy, J. (2018). UMAP: Uniform manifold approximation and projection for dimension  
477 reduction. *arXiv*, 1802(03426).
- 478 Mitchell, T., Shinkareva, S., Carlson, A., Chang, K., Malave, V., Mason, R., & Just, M. (2008). Predicting  
479 human brain activity associated with the meanings of nouns. *Science*, 320(5880), 1191.
- 480 Newman, M. E. J. (2005). A measure of betweenness centrality based on random walks. *Social Networks*, 27,  
481 39–54.
- 482 Newman, M. E. J. (2008). The mathematics of networks. *The New Palgrave Encyclopedia of Economics*, 2, 1–12.
- 483 Nishimoto, S., Vu, A., Naselaris, T., Benjamini, Y., Yu, B., & Gallant, J. (2011). Reconstructing visual  
484 experience from brain activity evoked by natural movies. *Current Biology*, 21, 1 - 6.
- 485 Nocedal, J., & Wright, S. J. (2006). *Numerical optimization*. New York: Springer.
- 486 Norman, K. A., Newman, E., Detre, G., & Polyn, S. M. (2006). How inhibitory oscillations can train neural  
487 networks and punish competitors. *Neural Computation*, 18, 1577–1610.
- 488 Opsahl, T., Agneessens, F., & Skvoretz, J. (2010). Node centrality in weighted networks: generalizing degree  
489 and shortest paths. *Social Networks*, 32, 245–251.
- 490 Pearson, K. (1901). On lines and planes of closest fit to systems of points in space. *The London, Edinburgh,  
491 and Dublin Philosophical Magazine and Journal of Science*, 2, 559-572.

- 492 Pereira, F., Lou, B., Pritchett, B., Ritter, S., Gershman, S. J., Kanwisher, N., ... Fedorenko, E. (2018). Toward  
493 a universal decoder of linguistic meaning from brain activation. *Nature Communications*, 9(963), 1–13.
- 494 Rao, C. R. (1982). Diversity and dissimilarity coefficients: a unified approach. *Theoretical Population Biology*,  
495 21(1), 24–43.
- 496 Ricotta, C., & Szeidl, L. (2006). Towards a unifying approach to diversity measures: Bridging the gap  
497 between the Shannon entropy and Rao's quadratic index. *Theoretical Population Biology*, 70(3), 237–243.
- 498 Rubinov, M., & Sporns, O. (2010). Complex network measures of brain connectivity: uses and interpreta-  
499 tions. *NeuroImage*, 52, 1059–1069.
- 500 Schreiber, T. (2000). Measuring information transfer. *Physical Review Letters*, 85(2), 461–464.
- 501 Simony, E., Honey, C. J., Chen, J., & Hasson, U. (2016). Uncovering stimulus-locked network dynamics  
502 during narrative comprehension. *Nature Communications*, 7(12141), 1–13.
- 503 Spearman, C. (1904). General intelligence, objectively determined and measured. *American Journal of  
504 Psychology*, 15, 201–292.
- 505 Sporns, O., & Honey, C. J. (2006). Small worlds inside big brains. *Proceedings of the National Academy of  
506 Science USA*, 103(51), 19219–19220.
- 507 Tipping, M. E., & Bishop, C. M. (1999). Probabilistic principal component analysis. *Journal of Royal Statistical  
508 Society, Series B*, 61(3), 611–622.
- 509 Tong, F., & Pratte, M. S. (2012). Decoding patterns of human brain activity. *Annual Review of Psychology*, 63,  
510 483–509.
- 511 Turk-Browne, N. B. (2013). Functional interactions as big data in the human brain. *Science*, 342, 580–584.
- 512 van der Maaten, L. J. P., & Hinton, G. E. (2008). Visualizing high-dimensional data using t-SNE. *Journal of  
513 Machine Learning Research*, 9, 2579–2605.
- 514 Zar, J. H. (2010). *Biostatistical analysis*. Prentice-Hall/Pearson.